Geophysical Journal International

Geophys. J. Int. (2022) **230,** 272–287
Advance Access publication 2022 February 23
GJI Geodynamics and Tectonics

https://doi.org/10.1093/gji/ggac073

Evolution of eastern segment of the Central India Tectonic Zone: an insight from a magnetotelluric study

Khasi Raju,[1] Prasanta K Patro,[1] Ujjal K Borah,[1,2] Shalivahan Srivastava[3] and K. Chinna Reddy[1]

[1] *CSIR–National Geophysical Research Institute, Uppal Road, Hyderabad* 500007, *India E-mail: patrobpk@ngri.res.in*
[2] *National Centre for Earth Science Studies, Ulloor—Akkulam road, Akkulam, Thiruvananthapuram* 695011, *India*
[3] *Indian Institute of Technology (Indian School of Mines), Dhanbad, Jharkhand* 826004, *India*

Accepted 2022 February 18. Received 2022 February 8; in original form 2021 February 27

SUMMARY

The collision process between the South Indian Block (SIB) and North Indian Block (NIB) resulted in the development of the complex crustal nature of the Central India Tectonic Zone (CITZ). The evolutionary past of CITZ covers a long geological time (∼1000 Ma), which corresponds to the assembly and spreading of Columbia and Rodinia supercontinents. Despite several studies in the western and central parts of the CITZ, the location of the suture zone between the SIB and NIB is still under debate. In addition to that, the crustal structure in the eastern segment of CITZ is yet to be resolved. Therefore, for the first time, a dense station coverage magnetotelluric (MT) study is carried out along a 275 km transect in the eastern segment of CITZ from Pandaria to Rewa. The complexity of the Central Indian Shear (CIS) and Tan Shear Zone (TSZ) are reflected as anomalous phases (beyond 90°) in the MT data. A deep crustal resistivity model derived from 2-D and 3-D inversion of the MT data brought out a high-to-moderate conductivity structure (10–100 Ω-m) in the middle of the surface expressions of CIS and TSZ. The conductive structure could be related to a deformation zone formed by tectonic interaction of the CIS and TSZ or multiple tectonic boundaries in the middle of the CIS and TSZ. The conductive structure observed in the southern limit of the CITZ also may indicate the tectonic boundary between the SIB and NIB. The high conductivity in the deformation zone may be explained by the collision-related metallic rich sediments and/or mylonite associated with interconnected fluids. Moderately conductive vertical features delineated from the MT model correlate with the intrabasinal faults which might have acted as the pathways for Deccan volcanism. This study suggests that the CITZ could have been developed under the transition of oceanic subduction to continental collision processes at multiple geological times.

Key words: Electrical properties; Asia; Magnetotellurics; Crustal structure.

1 INTRODUCTION

Merging of South Indian (Dharwar, Bastar and Singhbhum cratons) and North Indian (Bundelkhand craton) blocks during Neo Archaean–Palaeoproterozoic time resulted in the Central India Tectonic Zone (CITZ, Fig. 1a). It is covered with different litho-tectonic units covering the Archaean, Proterozoic and Phanerozoic ages (Naqvi *et al.* 1974; Acharyya & Roy 2000). Deep-seated faults/shear zones such as the Narmada–Son lineament (NSL), Tan Shear Zone (TSZ) and Central India Shear (CIS) zone are the main tectonic boundaries in the CITZ that evolved during the collision process and they act as a zone of crustal weakness. The CITZ also consists of intrabasinal faults such as Balarampur–Tattapani Fault (BTF) and Balaghat–Chilpand Fault (BCF, Fig. 1b). The NSL in the north and CIS in the south define the northern and southern boundaries of CITZ. The NSL is bounded by the mantle reaching Narmada–Son North Fault (NSNF) and the Narmada–Son South Fault (NSSF, West 1962; Choubey 1971). Reactivation of the NSSF led to the deposition of the South-Rewa Gondwana basin in the southern part of the fault (Chakraborty *et al.* 2003), while reactivation of the NSNF led to the Vindhyan sedimentation to the north of NSL (Kaila *et al.* 1987). Many geological and geophysical investigations have been carried out so far to explore such complicated tectonic settings of the CITZ. However, the conflicts over subduction polarity and location of the suture zone between the South Indian Block (SIB) and North Indian Block (NIB) are yet unsettled. Several studies (Jain & Yedekar 1989; Yedekar *et al.* 1990; CRUMANSONATA 1995; Mishra *et al.* 2000; Acharyya 2003) suggest that the two cratonic blocks (SIB and NIB) are sutured by the southward subduction of the NIB underneath the SIB. Others (Roy & Prasad 2003; Mall

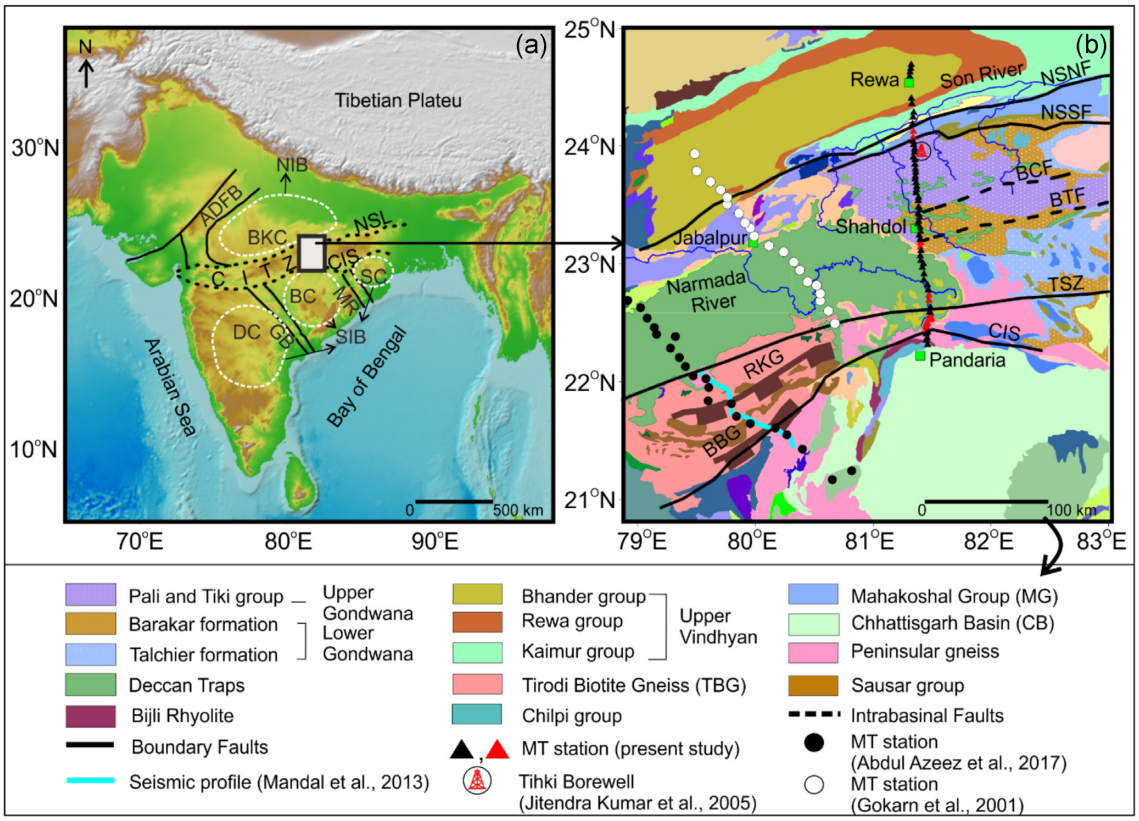

Figure 1: (a) Topography (source: https://www.gmrt.org/GMRTMapTool/) map of India showing the cratons and suture zones of the Indian subcontinent. The major tectonic boundaries are indicated by the black colour thick and dash line. (DC—Dharwar Craton, BC—Bastar Craton, SC—Singhbhum Craton, GB—Godavari Basin, MR—Mahanadi Rift, CIS—Central India Shear, NSL—Narmada–Son Lineament, BKC—Bundelkhand Craton, ADFB—Aravalli–Delhi Fold Belt, CITZ—Central India Tectonic Zone). SIB includes Bastar, Dharwar, and Singhbhum cratons and NIB comprises of Bundelkhand craton sutured along the CITZ. The white colour rectangular box in the figure represents the location of the present study area. (b) Detailed geological and tectonics map of the Rewa–Pandaria region (GSI 2005; Dotiwala & Pangtey 1997; Bhowmik 2019). The intrabasinal and boundary faults (BTF and BCF) of Gondwana basins are plotted on the map. Current MT station locations are plotted in black-filled triangles (MT phase in the quadrant) and red-filled triangles (MT phase-out of the quadrant). Previous MT studies are indicated with a black filled circle (Abdul Azeez *et al.* 2017) and white filled circle (Gokarn *et al.* 2001) [NSSF: Narmada–Son South Fault, NSNF: Narmada–Son North Fault, CIS: Central India Shear, TSZ: Tan Shear Zone, BTF: Balarampoor–Tattapani Fault, BCF: Bahmni–Chilpaand Fault, RKG: Ramakona-Katangi Granulite and BBG–Bhandara–Balaghat Granulite].

et al. 2008; Rao *et al.* 2011; Mandal *et al.* 2013; Abdul Azeez *et al.* 2013) indicate that the SIB subducted below the NIB which sutures two blocks. In addition, geological and geophysical investigations (Yedekar *et al.* 1990; Jain & Yedekar 1989; CRUMANSONATA 1995; Mishra *et al.* 2000; Mall *et al.* 2008; Rao *et al.* 2011; Mandal *et al.* 2013) suggest that the CIS represents a suture zone between the SIB and NIB. According to other studies (Chattopadhyay & Khasdeo 2011, Abdul Azeez *et al.* 2017; Chattopadhyay & Bhattacharjee 2019; Chattopadhyay *et al.* 2020), the SIB and NIB are sutured together along the TSZ.

Magnetotellurics (MT) is an effective passive electromagnetic (EM) method to image the crustal and lithospheric structure with the inherent nature of deeper penetration of the MT signal at lower frequencies. The MT response is sensitive to even small changes in highly conductive rocks and minerals such as graphites, sulphides which follow different conduction mechanisms and interconnected fluids (Unsworth *et al.* 2005, Camfield & Gough 1977; Korja & Hjelt 1993; Pous *et al.* 2004). Previous MT studies across the CITZ delineated several electrical conductors that are associated with ancient major faults zone in the CITZ (Gokarn *et al.* 2001; Rao *et al.* 2004; Patro *et al.* 2005; Naganjaneyulu & Santosh 2010; Abdul Azeez *et al.* 2013; Patro & Sarma 2016; Abdul Azeez *et al.* 2017). These vertical conductors connected with faults are interpreted as mafic material associated with fluids. These conductors act as weak zones through which magma enters and moved towards the upper crust during the Deccan volcanism (Patro & Sarma 2016). It is important to note that most of the earlier geophysical studies, including MT, were carried out in the western and central parts of the CITZ to understand the tectonics and delineate the deeper structures. However, the deep electrical image of the eastern segment of the CITZ is not available yet. Therefore, this study aims to image the eastern segment of CITZ covering the South-Rewa basin, Vindhyan basin and major tectonic features such as CIS, TSZ and NSL (see Figs 1a and b) to understand the tectonics associated with the collisions process between the SIB and NIB.

2 GEOLOGICAL SETTINGS

The study area is situated in the eastern segment of the CITZ, covering Madhya Pradesh and Chhattisgarh states. The southernmost part of the study area comprises the Proterozoic Chattisgarh Basin (CB), deposited over the ∼2.5 Ga granitoids of Bastar craton (George & Ray 2020). Proterozoic origin of schist belts, that is, Chilpi Group occur in linear belts in the northern part of CB (Fig. 1b). The Chilpi Group comprises of conglomerate, coarse arenite (grit), shale and

quartzite, and it overlies the Palaeoproterozoic Nandgaon Group of rocks (a subgroup of the Dongargarh Supergroup, Sharma *et al.* 2014). Palaeoproterozoic Bijli Rhyolite in the Nandagaon Group occurs in the north of the Chilpi group, is one of the most voluminous silicic volcanic expressions in the Indian Shield. The Bijli Rhyolite is a product of crust–mantle interaction where crustal mobilization took place at various crustal depths during the Archaean–Palaeoproterozoic period (Sensarma *et al.* 2004). The CIS marks the northern limit of Bijli Rhyolite and Archean Peninsular Gneiss (Bastar craton) that occurs along with the CIS (Fig. 1b). The region between the CIS and BTF is covered with the Cretaceous-Tertiary Deccan Basalt emplaced through the ancient zones of structural weakness in the CITZ (Bhattacharji *et al.* 1996). The Late Cretaceous Lameta beds consist of limestone, sandstone, clay and shales (CRUMANSONATA 1995; Srivastava & Mankar 2015) occurs as a linear belt in the middle of Deccan traps and South-Rewa basin.

Lower Gondwana formations such as Talchir, and Barakar cover the area in between the BTF and BCF. The area between the BCF and NSSF is occupied mostly by the Upper Gondwana formation of the South-Rewa basin. The basin is controlled by BTF and NSSF on south and northern limit respectively, and that comprises Pali formation, Karki formation, Tiki formation and the unconformably overlying Parsora formation (Mukherjee *et al.* 2012). The chief rock formations of the South-Rewa Gondwana basin are sandstone, shale, conglomerate and mudstone (Casshyap *et al.* 1993; Chakraborty *et al.* 2003). Mafic dykes of Deccan volcanic province intruded in the middle of the Gondwana basin, and the trend of dykes varies from NW-SE to NE-SW (Lala *et al.* 2011). Metavolcanic and metasedimentary rocks of Mahakoshal group (MG) of supracrustal rocks expose as a linear belt in the middle of NSSF and NSNF. The supracrustal rocks are deposited over the granitic gneissic basement in a narrow fault-controlled linear basin. The rocks are intensely deformed and contain post-tectonic intrusions such as granitic and ultramafic plugs. The Gondwana group and mylonite belt contact the MG on its southern margin (Roy & Prasad 2001).

The northern part of the MG is bounded by the Vindhayn Supergroup of rocks except around the Sidhi area, where gneissic granite occurs in a linear belt (CRUMANSONATA 1995). The study area north of NSNF is occupied by the Vindhyan Supergroup of the Upper Proterozoic age (see Fig. 1b). The Supergroup is divided into the lower Vindhyan of the Semri Group, the upper Vindhyan of the Kaimur Group, the Rewa Group and the Bhander Group (Fig. 1b, Kumar & Sharma 2012). The Semri is the oldest group of the Vindhyan formation in the Son valley area that rests on granites and metamorphic rock. The upper Vindhyan of Kaimur, Rewa and Bhander groups lay on the Semri group subsequently (Chakraborty 2006).

3 MAGNETOTELLURIC METHOD

MT is a passive EM method which utilizes a wide spectrum of natural EM fields (originated from ionospheric currents and worldwide thunderstorm activity) to delineate the subsurface electrical structure of the earth. The low-frequency (<1 Hz) natural EM fields are generated by Earth's ionospheric currents, and the high-frequency fields (>1 Hz) occur from the global thunderstorm activity associated with lightning events. The time-varying magnetic and electric fields along two mutually perpendicular directions are measured on the earth's surface and related them via a complex impedance tensor (Z). The Z is a second rank complex tensor which can be represented in the frequency domain as (Simpson & Bahr 2005):

$$\mathrm{E} = \mathrm{ZH} \text{ or } \begin{pmatrix} \mathrm{E_x} \\ \mathrm{E_y} \end{pmatrix} = \begin{pmatrix} \mathrm{Z_{xx}} & \mathrm{Z_{xy}} \\ \mathrm{Z_{yx}} & \mathrm{Z_{yy}} \end{pmatrix} \begin{pmatrix} \mathrm{H_x} \\ \mathrm{H_y} \end{pmatrix}. \quad (1)$$

Where E_x, E_y are the electric field components; H_x and H_y are the components of magnetic induction along two mutually perpendicular directions x and y; (x, y) preferably denotes geographic north and east respectively. The Z is frequency dependent and complex, and generally represented in terms of amplitude (apparent resistivity, ρ_a) and phase lag (φ) between electric and magnetic fields. At a particular frequency (f) ρ and φ can be represented in terms of Z as (Weckmann *et al.* 2003a; Hering *et al.* 2019):

$$\rho_{\mathrm{a,\ xy}} = \frac{\mu_0}{2\pi \mathrm{f}} \left|\mathrm{Z_{xy}}\right|^2, \quad (2)$$

and

$$\varphi = \tan^{-1}\left(\frac{\mathrm{Im}\left(\mathrm{Z_{xy}}\right)}{\mathrm{Re}\left(\mathrm{Z_{xy}}\right)}\right). \quad (3)$$

Where μ_o is the magnetic permeability of free space.

4 MT DATA

MT data were collected at 69 locations between 2014 and 2016 using the ADU-07e system (M/s Metronix, Germany) along a 275 km long profile across the Rewa-Pandaria region. At each station, we have recorded the three mutually perpendicular magnetic field components (H_x, H_y and Hz) and two perpendicular horizontal electric field components (E_x and E_y) simultaneously using induction coil magnetometers and non-polarized electrodes, respectively. The MT data are collected in the frequency range of 65k Hz to 0.001 Hz with sampling frequencies 65536, 4096, 1024, 512, 128 and 32 Hz. We have recorded multiple data sets for each sampling frequency with different gains to improve the signal-to-noise ratio. For most of the profile, MT station spacing is maintained at 4–5 km; however, in the areas of major tectonic boundaries (such as CIS, TSZ), the interstation distance is reduced to 0.5 km. One remote station is maintained for the entire field season to enable remote reference processing, which can improve the base station data quality when the noise is affected severely (Gamble *et al.* 1979).

MT data are processed using the MAPROS software (M/s Metronix, Germany). Due to the constraint in selecting the MT sites, a few of them are set up near the state highways and major towns such as Shahdol, Rewa. Hence, the MT data at a few locations are affected by cultural noise as well as power line noise. Therefore, before processing the MT data, we have visually checked the time-series data to remove the unwanted portions, that is, spike and burst. Later on, a notch filter is applied to remove the 50 Hz power line frequency. After removing the unwanted signal from time-series data, we process the data using different approaches such as selecting stacking, coherency threshold, stack all and remote reference method as suggested in Borah et al. (2015) for an improved MT transfer function.

The consistency of the processed MT data set can be ascertained using the D+ parameter that seeks to find the best fit for apparent resistivity and phase parameters (Parker 1983; Beamish & Travassos 1992). Therefore, the present data set robustness is examined with the D+ parameter (added 10% error). A major portion of the data set shows consistency in the apparent resistivity and phase (Fig. 2). Pseudosection plot of apparent resistivity and phase data are presented in Fig. 3.

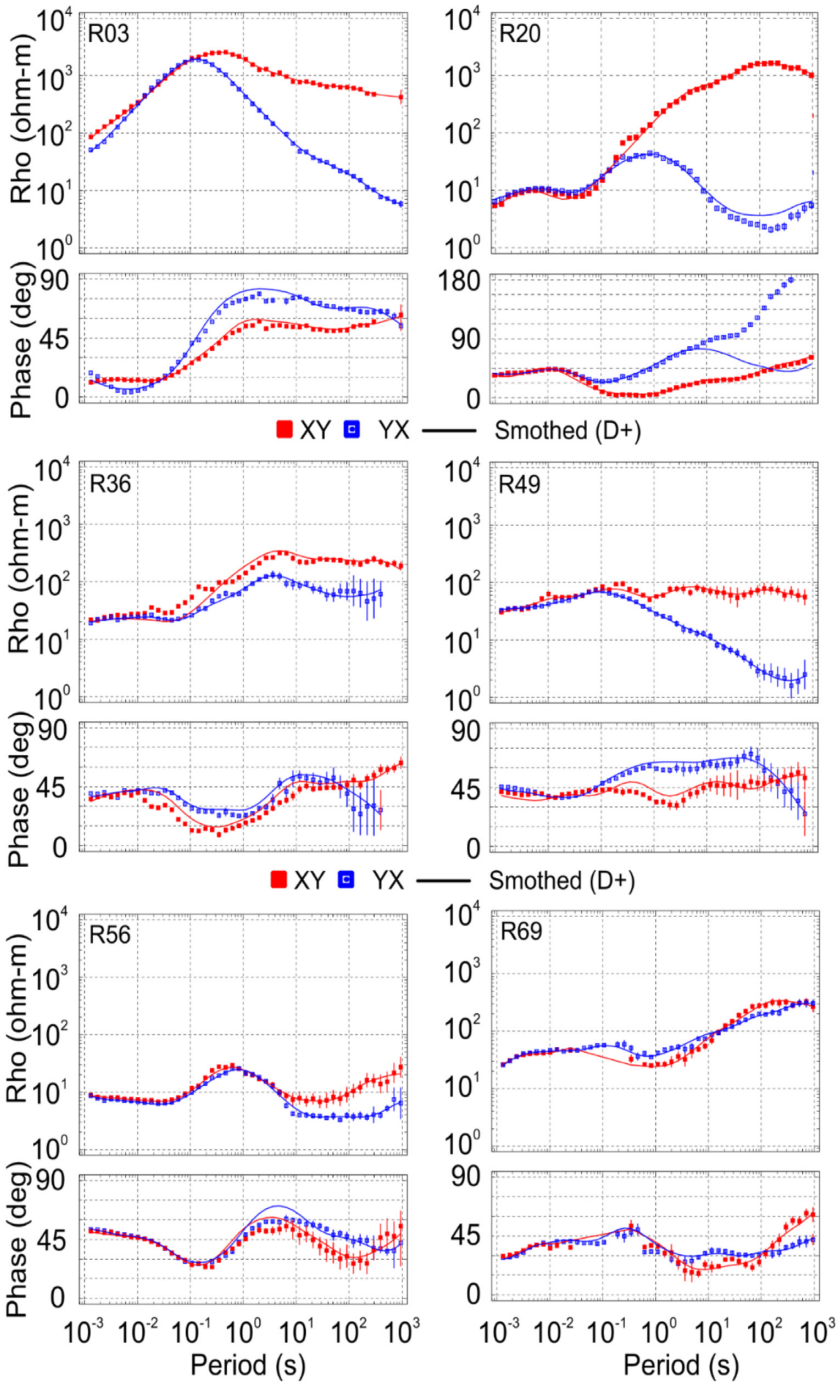

Figure 2: MT transfer functions are plotted for a few locations spreading over different geological terrains in the Rewa-Pandaria region. The D+ smoothing parameter for the *XY* component (red colour thick line) and *YX* component (blue colour thick line) was computed for each station to examine the consistency/robustness of the data set.

5 DIMENSIONALITY ANALYSIS

Examination of dimensionality of the MT data is an essential step to determine which type of modelling, that is, 1-D or 2-D, or 3-D, is adequate to estimate the subsurface resistivity structure (Simpson & Bahr 2005; Chave & Jones 2012). In this study, we consider Bahr skew and phase tensor (PT) parameters to analyse the dimensionality of the MT data. Estimation of phase-sensitive skew (η) for the present MT data set shows low skew values ($\eta < 0.1$) up to 10 Hz for the entire profile (as shown 'A', Fig. 4a) except for the CIS and NSL zones. The low skew values ($\eta < 0.1$) in that frequency range represent a 1-D or 2-D structure (Bahr 1988 1991). At the low-frequency range (<10 Hz), the η shows high values ($\eta \geq 0.3$) at most of the sites that suggest a 3-D nature of the subsurface (Bahr 1988 1991), except at the frequency range shown as 'B' in Fig. 4(a) show the low skew ($\eta < 0.3$) values. However, even these low skew values may also represent a 3-D (Ting & Hohmann 1981; Marti *et al.* 2009; Chave & Jones 2012). The PT plot (Fig. 4b) shows uniform circles and zero skew angle (β) value up to 10 Hz that in-

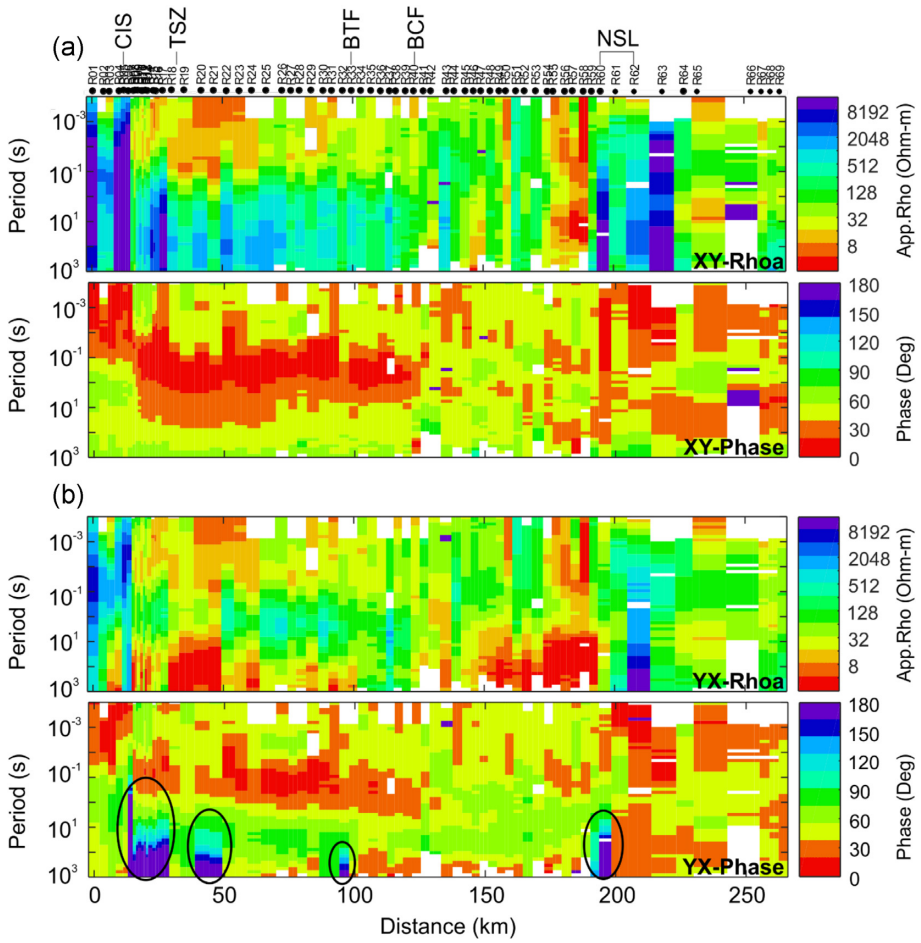

Figure 3: Pseudo-section plot of (a) XY and (b) YX components of apparent resistivity and phase data along the MT transect. Black ellipses in the YX phase pseudo-section indicate the anomalous phase data at a few MT stations along the MT traverse.

dicates a 1-D subsurface (Caldwell *et al.* 2004) for the entire profile except in the CIS and NSL region (Fig. 4b). Non-zero values of PT skew angle (β) and asymmetrical shape of PT ellipses are observed for the entire frequency range in the CIS and NSL zone as well as for the lower frequency range (<10 Hz) in the entire study area. The anomalous skew (η and β) values, as well as the asymmetrical shape of the PT, suggest that the region has undergone intense tectonic activity. Mohr circle analysis of these data set also suggests the complex nature of the subsurface beneath CITZ (Raju & Patro 2020).

6. ANOMALOUS PHASE

A total of 18 MT stations along the profile (red colour triangle in Fig. 1b) exhibit phases beyond 90° (see Fig. 3 and Fig. S5, Supporting Information). The MT stations, in the southernt and northern parts of the study area, show the anomalous phase from 10 s except at the R06 station, where the anomalous phase starts at 0.1 s. The MT stations (R31 and R32) in the middle of the traverse show the phase beyond 90° at 100 s. Usually, the MT phase should be between 0° to 90° for a 1-D or 2-D structure (Weidelt & Kaikkonen 1994). However, current channelling and anisotropy critically distort the MT curves in a complex geological condition, reflecting anomalous phase values (>90°). Earlier, many studies interpreted the anomalous phase behaviour with the connection of 3-D (e.g. L-shaped body, high conductive ring structure, etc.) structure (Egbert 1990; Livelybrooks *et al.* 1996; Pous *et al.* 2004; Weckmann *et al.* 2003b; Ichihara & Mogi 2009). The location of the anomalous phase MT station spatially coincides with major lineament/ fault zone such as the CIS, TSZ, BTF and NSL. Thus, the surficial heterogeneity or subsurface anisotropy across the tectonic boundaries could be a cause of an anomalous phase in the present data set. We examine the present data set using phase difference, PT and induction vector to identify whether MT data encounter electrical anisotropy or not (for more details see Section S2 in the Supporting Information).

High phase difference observed in MT data at several isolated areas (Fig. S6, Supporting Information) suggests heterogeneity in the crust. The area where PT major axis is aligned normally to the regional strike direction (Fig. S7, Supporting Information) coincides with the high phase difference, and weak ellipticity of PT (Fig. S7, Supporting Information) along the profile does not favour crustal anisotropy in the study area (Yin *et al.* 2014, and references therein). In addition, the consistent direction of the real part of induction vectors (Fig. S8, Supporting Information) indicates the presence of crustal heterogeneity accompanied by modified 2-D structures (Weidelt 1999; Heise & Pous 2003; Weckmann *et al.* 2003b; Marti 2014). From the above results, we suggest that the high phase difference across the major tectonic boundaries could be associated with regional crustal heterogeneity or distortion due to the near-surface 2-D or 3-D structures. Hence, the presence of anisotropy in the study area is ruled out.

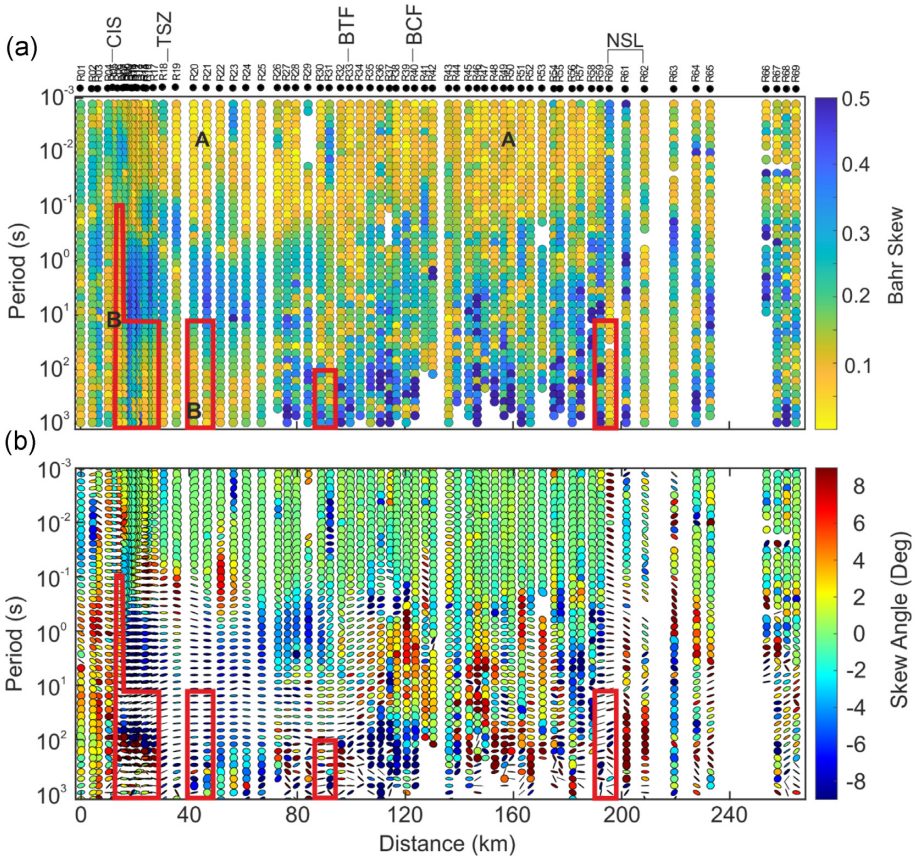

Figure 4: (a) Graphical representation of Bahr skew computed for all the sites. Low skew values are observed in the high-frequency range (marked as A), indicating the 1-D nature of the subsurface. In the lower frequencies, high skew values are observed, indicating the 2-D/3-D nature of the subsurface. At a few pockets in the lower frequencies, the skew values are observed low (marked as B in the figure). (b) The PT ellipses are plotted for all the sites. The colour of the ellipse represents the PT skew. The data set having anomalous phase ($> 90°$) are shown in red blocks in the above figure.

7. INVERSION OF MT DATA

7.1. 2-D inversion

2-D inversion of the MT data from 62 stations (TE+TM+Tz) in the frequency range of 1000–0.001 Hz was carried out using the nonlinear conjugate gradient (NLCG) algorithm of Rodi & Mackie (2001), which is implemented in the WinGlink software package. The 2-D model was created with 41 rows and 451 columns. The inversion was carried out using a homogeneous half-space of 100 Ω-m as starting model. The mesh for inverting the MT data has a thickness of the first row of 52 m which increases with a factor of 1.5. As the elevation in the southern segment of the traverse is ∼ 1016 m, we have included topography in the inversion. The regularization parameter (τ) plays a critical role that balances the data fit and the smoothness of the model. Larger τ values generate smooth models with larger data misfits, whereas smaller τ values yield rough models with smaller data misfits. We perform the inversion with different τ values ($\tau = 1, 2, 3, 5, 7, 10, 15, 30, 50, 100$) to find the optimal choice between roughness and the root mean square error (RMS) as a measure of data fit. Based on the results, $\tau = 10$, which falls in the knee of the curve (Fig. 5), is considered as an optimal value for the 2-D inversion. Here, we have used the standard grid Laplacian operator for the inversion. Error floor laverages the influence of data points with large individual errors that might occur in particular at long periods which are statistically less robust. A uniform error floor of 20 per cent for the apparent resistivity and

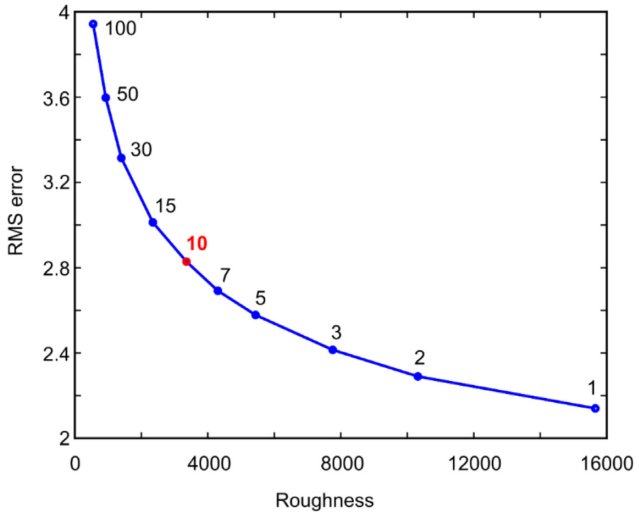

Figure 5: The L-curve is generated to define the suitable smoothing parameter (τ) for the 2-D full tensor inversion. Where $\tau = 10$ is considered as the best smoothing parameter for the 2-D model.

5 per cent for phase (1.45°) is assigned to both TE and TM data. The error floor of 0.1 per cent was assigned to the tipper in the 2-D inversion. A higher error floor in apparent resistivity over the phase values is considered to account for static shift effect in the data

(Ogawa 2002). The final model obtained after 300 iterations (RMS = 2.76) is presented in Fig. 6. We have also carried out the 2-D inversion using the uniform grid Laplacian operator (see Fig. S10, Supporting Information). Both standard and uniform grid models reveal similar subsurface features except the feature C3, which is very weak in the uniform grid model. A good data fit is noted between observed and calculated responses (Fig. S11, Supporting Information). For comparison, we also inverted the TM and Tipper data for the frequency range 1000–0.001 Hz. The final model is presented in Fig. S12 in the Supporting Information.

The robustness of the different electrical conductivity features that are obtained through 2-D inversion is evaluated using sensitivity studies. Before evaluating the subsurface features, we have computed Bostick transformation depth (Bostick 1977; Jones 1983) for each station to estimate the depth of penetration (Fig. 7). It may be seen that most of the stations show more than 50 km penetration depth except a few MT sites in the Gondwana sediment region. Therefore, we restrict our present model to 30 km for geological interpretation. The conductors (C1–C6) are replaced with neighbouring resistivity values 100 and 10000 Ω-m and subsequently we computed forward responses. The results are correlated with the observed and calculated data at the MT stations corresponding to the conductors (Fig. S13, Supporting Information), and we note a substantial deviation between the forward and inversion responses at the C1–C6 conductors. However, we observe that the bottom of the conductor C5 is not resolved (see Fig. S13, Supporting Information).

The 2-D conductivity model (Fig. 6) revealed several conductive anomalies, some of which can be correlated with known structural features such as CIS, BTF, BCF and NSL. In the southern part, CIS correlates with the moderate conductor (∼10 Ω-m) that dipping towards the south (C1). The conductor C2 (∼1 Ω-m) is noted in the mid-crustal level, however, that does not correspond to any surface signature. The BTF (C3 in Fig. 6) is spatially associated with a moderate conductive structure (∼100 Ω-m) that separates the high resistivity segments in the near-surface. In the lower crustal level, the surface expression of BTF is well correlated with the high conductive structure (∼1 Ω-m). In the middle part of the 2-D resistivity model, the vertical conductors (C4 and C5) spatially correlated with intrabasinal faults in the South-Rewa Gondwana basin. In the northernmost segment, the surface exposure of Vindhyan sediments coincides with the low resistive (10–30 Ω-m) layer at a shallow level.

7.2. 3-D inversion of MT data

Since in the 2-D inversion, we could not use all the data from the southern segment due to anomalous phase (see Fig. 3 and Fig. S5, Supporting Information), and due to higher dimensionality at a few periods along the profile, we further carried out 3-D inversion of the MT data. For that, we have used the modular EM 3-D inversion code ModEM (Egbert & Kelbert 2012; Kelbert et al. 2014), which is based on an NLCG algorithm. Close spacing (0.5 km) between the MT stations in the southern segment of the profile limits the 3-D mesh construction. Therefore, we considered 62 MT stations (removed seven stations data in the southern part) data for 3-D inversion. Also, we considered 62 stations data for 2-D inversion in order to correlate both inversion results. The mesh was setup with the coordinate system of x (north), y (east) and z (depth). The 3-D mesh consists of 169, 43 and 58 grids in the x, y and z directions, respectively. Topography (10 layers) and bathymetry of the Bay of Bengal (source: https://maps.ngdc.noaa.gov) which is situated nearly 500 km away from the profile in the SE direction is included in the model mesh. The core area of the model space was gridded finely with a node spacing of 1.96 km in the X-direction (north–south) and Y-direction (east–west) to have a good resolution of the horizontal resistivity variations. The model grid is shown in Fig. 8. A total of 17 padding layers were used around the core grid area and the width of the padding was increased progressively by a factor of 1.3. In the vertical direction, a 50 m first layer was considered and the subsequent layers were increased by a factor of 1.2 of the previous layer until a total model depth of about 1579.28 km. The final model mesh is about 1718 × 1471 × 1896 km. The model covariance used in X, Y and Z directions is 0.2, 0.4 and 0.2, respectively. We used all the 62 MT stations full tensor (Z_{xx}, Z_{xy}, Z_{yx}, Z_{yy}) and 61 stations tipper (T_{zx}, T_{zy}) data with 46 frequencies from 0.001 to 1000 s in the 3-D inversion. Some of the outliers from the observed data were removed from inversion. Data errors were used with error floor as 5 per cent of sqrt ($|Z_{xy}$ x $Z_{yx}|$) for all the impedance components, and for tipper, 0.05 per cent of T_{zx} and 0.05 per cent of Tzy were assigned. We have studied the non-uniqueness problem of 3-D inversion by assigning different half-space initial models with resistivity values of 10, 100 and 1000 Ω-m. The inversion (see Fig. 9) reveals some major conductive and resistive features with the RMS values as 2.93, 2.75 and 2.11, respectively. Since the RMS for the 1000 Ω-m half-space initial model is the minimum as compared to the other two models, we have considered it as the preferred model and presented it in Figs 10(b) and (c). The data fit of observed and modelled responses are shown in Figs S14 and S15 in the Supporting Information, and normalized RMS misfit for each station is shown in Fig. S17 in the Supporting Information.

The full tensor with tipper inversion results of the deep 3-D resistive structure is presented in shallow (up to 8 km) and deeper sections (30 km) as shown in Figs 10(b) and (c). The shallow 3-D section is presented here only to delineate the Gondwana and Vindhyan sediment thickness, and we note ∼100 Ω-m resistive structure at near-surface that spatially correlate with the Deccan Basalt layer on the surface. Depth to the basement computed from 1-D inversion is plotted as black colour dashed line on the shallow 3-D model (Fig. 10b). We observe a good agreement between the conductive features in the 3-D model and sediment thickness from 1-D inversion. In the deeper section (Fig. 10c), the region between the CIS and TSZ is characterized by a high conductive (< 10 Ω-m) feature (C1 in Fig. 10c) starting from the upper crust, and it extends to the lower crust as a moderate conductive feature (∼ 100 Ω-m). High resistive segments (R1 and R2 in Fig. 10c) are observed on both sides of the conductive feature (C1). In the middle part of the 3-D model, the vertical moderate conductive structures (C3 and C4 in Fig. 10c) are delineated. They coincide with the surface expression of intrabasinal faults, that is, BTF and BCF. Below the surface expression of Gondwana sediments, the 3-D resistive model brought out discrete conductive bodies, such as C6 in Figs 10(b) and (c). Further north, the region between the NSSF and NSNF is characterized by a low to moderate resistive (10–100 Ω-m) structure (see C7 in Figs 10b and c). In the northernmost part of the model, the high resistive structure near the surface may be a signature of an artefact that could be generated due to the data gap. Horizontal depth sections are presented in Fig. 11. The conductive features C1 and C3 show extension as deep as 28–34 km depth range. As we go deep the off-profile extension of these features are observed. Conductive features C7 and C8 are observed below the profile at shallow depths (5–8 km), but disappear from the profile with increasing depth.

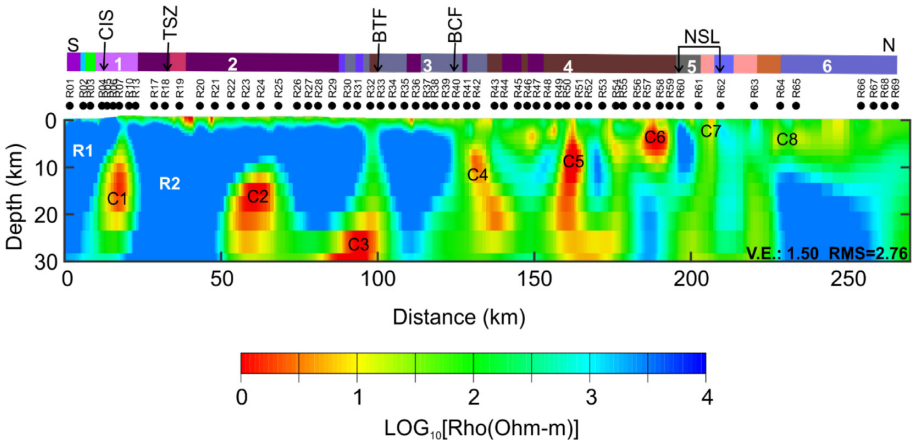

Figure 6: Deep geoelectric section derived from the 2-D inversion of the MT data (TE+TM+Tz) in the frequency range of 1000–0.001 Hz. The 2-D inversion is carried out using the NLCG algorithm of Rodi & Mackie (2001). The finite-difference fine mesh incorporated 451 columns and 41 rows are used for inverting the TE+TM+Tz data. The top panel shows the geology of the study area. 1: Peninsular gneiss, 2: Deccan trap, 3: Upper Gondwana, 4: Lower Gondwana, 5: Mahakoshal and 6: Vindhyan.

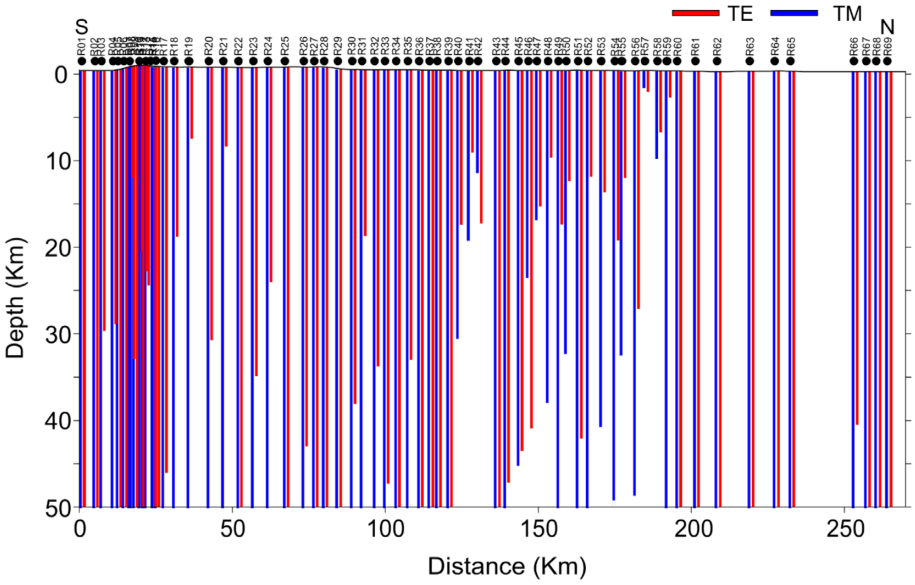

Figure 7: Bostick depth transform of TE and TM components for each station along the MT profile.

The robustness of conductors C1, C3, C4 and C6 in the 3-D model is examined using sensitivity analysis. We tested by masking each conductor with the resistivity values of the adjacent resistivity and then computed the forward response. Such an approach was carried out for all the conductors. Computed response and forward responses are compared for the stations above these conductors. We note a significant variation between the inversion and forward responses (see Fig. 12). This study confirms the necessity of these conductive features in the model.

7. 4. Correlation of 2-D and 3-D inversion results

We note a substantial difference between the 2-D and 3-D inversion results particularly in the southern segment of the profile. Where the 2-D model brought out high conductive (∼1 Ω-m) structures C2 and C3 as shown in Fig. 6. While conductor C2 did not appear in the 3-D model, conductor C3 has a presence with moderate amplitude. The sensitivity analysis of these two conductors (C2 and C3) suggests that they are sensitive only in the TE component (see Fig. S13, Supporting Information). We further carried out the 2-D inversion of the synthetic MT data derived from the 3-D inverted model. It also brought out a few unrealistic high conductive regions especially in the southern segment of the profile (see Fig. S16, Supporting Information). The off-profile structure is another possibility of the occurrence of unrealistic high conductive structure in the 2-D model (e.g. Cruces *et al.* 2020). However, PT and induction vector analysis do not reflect a signature of off-profile structures. In addition to that, in the present 3-D model also we do not note off-profile structures corresponding location of the conductor C2 in the 2-D model (see Fig. 11). We observe similar features in 2-D and 3-D models for the rest of the profile. The similarity between the 2-D and 3-D results may be occurred due to the finite strike length of a 3-D structure below the profile or induction scale length may be less than the 3-D structural length. The conductive structures are observed in the 2-D model more conductive than those are noted in the 3-D model (e.g. see C4 in Figs 6 and 10). Besides, the conductors (C4 and C5 in Fig. 6) in the 2-D models are extended more depth

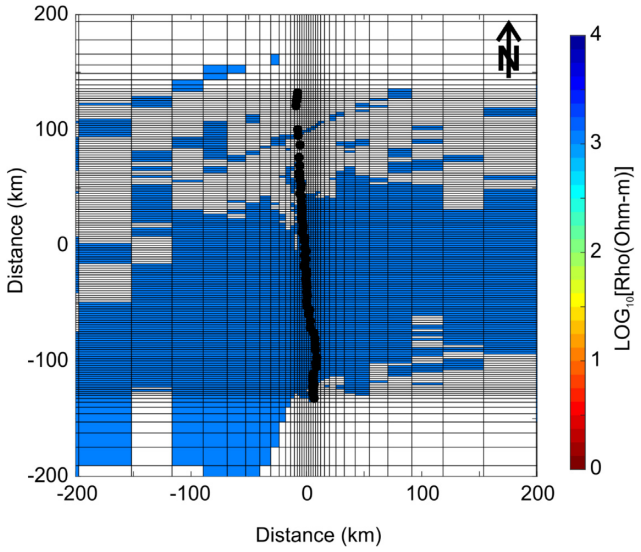

Figure 8: Horizontal view of 3-D mesh setup for inverting measured data in the study area. The MT station locations are plotted as black colour circle. Topography is included into the model. The blank regions in the model grid represents as air layer.

compared to the 3-D model. To improve the data fit in the lower frequency, the conductors' roots may be extended to deeper depth also reduce resistivity values in the 2-D inversion (e.g. Siripunvaraporn, *et al.* 2005). The above assumption is well supported by the lack of robustness of the conductor C5 lower edge in the 2-D model.

8. DISCUSSIONS

8.1. South-Rewa Gondwana basin and intrabasinal faults

Gondwana sedimentary formations in India are formed along the Proterozoic mobile belt during the crustal resetting process. The South-Rewa Gondwana basin is considered an intra-cratonic rift basin that was developed under the NNE-SSW trending extensional tectonic regime (Acharyya 2019). However, what controls the formation of a rift basin is a crucial question. Active and passive continental rift is generated under the influence of extensional tectonics; however, the main difference is in the emplacement of mantle material. In general, the horizontal movement of the plate generates a passive rift, while the mantle plume is the causative factor for active rift (Ruppel 1995). The active rifting is characterized by crustal doming and abundant flood basalt during the early stage with graben formation and sedimentation later stage. Whereas the 'passive' rifting exhibits graben formation and marine sedimentation in the first stage, followed by volcanism in the later stage (Merle 2011).

Upward migration of molten upper mantle material gives rise to local extensional stress in the lithosphere, and that may be accompanied by NNE-SSW trending regional extension tectonic stress on the Indian plate. Local and regional extensional stress together leads to the thinning of the lithosphere in central India, and later on, develop an active NSL rift structure in the backarc region of NIB. Below the NSL rift zone, MG supracrustal rocks (C7 in Figs 10b and c) are emplaced in the crustal level during the rift evolution (Acharyya & Roy 2000). Also, the basement uplifted and granite rocks intruded along the weak zone (Chattopadhyay *et al.* 2020). Later on, the continuous sinking of faults brought out a graben structure on either side of the NSL to deposit Gondwana and Vindhyan sedimentation.

The present geo-electrical 3-D model delineates the South-Rewa Gondwana sedimentary structure with a resistivity range of 10–30 Ω-m (e.g. see C6 in Fig. 10b) on the southern side of NSL. We have also carried out a 1-D inversion of invariant ($\frac{1}{2}$ $(Zxy + Zyx)$) component of MT data using Occam inversion scheme (Constable *et al.* 1987). The 1-D modelling results show the thickness of the sedimentary column gradually decreases either side of the basin as shown in black colour dashed line in Fig. 10(b). Correlation of 1-D derived sediment thickness with the shallow 3-D model suggests that the South-Rewa basin sediments are deposited in faults bounded full graben depression, which is controlled by the BTF and NSL in the south and northern parts respectively. Maximum thickness of sediment (∼5 km) is noticed near to the NSL that is well correlated with the Tikhi Borewell location (Jitendra Kumar *et al.* 2005) as shown in Fig. 10(b). The sedimentary thickness and tectonic setting of the South-Rewa basin indicate that the northern part of the basin is prospective compared to the southern region. In the northern part of NSL, the conductive layer (10–30 Ω-m) coincides with the Vindhyan sedimentary column. Its thickness increases towards the NSNF as noted with a black colour dashed line which is derived from 1-D inversion. From the 1-D and 3-D modelling results, we suggest that the Vindhyan sediments may be deposited in a half-graben structure which was evolved during the formation of the NSL rift zone as the sediment thickness increases continuously towards NSL as shown in Fig. 10(b).

The present 3-D model also images moderate conductors (50–100 Ω-m) in the middle part of the study area (C3 and C4 in Fig. 10c) which are spatially correlated with intrabasinal faults, that is, BTF and BCF in the South-Rewa basin. Earlier MT studies (Rao et al 1995; Gokarn *et al.* 2001; Rao *et al.* 2004; Patro *et al.* 2005; Naidu & Harinarayana 2009; Abdul Azeez *et al.* 2013; Patro & Sarma 2016) in the central and western part of the CITZ delineate the discrete conductive bodies (10–100 Ω-m) in upper to lower crustal level, and they suggested that mafic material associated fluids being an agent for high conductivity in the CITZ. During the Deccan volcanism, mantle origin mafic material erupted through the weak zones in central India and underwent a prograde metamorphism reaction. Heat associated with the prograde metamorphism dehydrates the rocks, and a huge amount of fluid generates (Frost & Bucher 1994). Migration of these fluids with magma through the weak zone of the crust evolved as CO_2-rich fluid (Frost & Frost 1987). At the average crustal temperature of 400 °C, fluids continue to exist for 0.1–1 Ga (Jones 1992). Therefore, it may be inferred that the mantle-derived mafic-ultramafic materials associated with the metamorphic origin of fluid are responsible for the high conductivity in the crustal range. The moderate conductive structure (50–100 Ω-m) below the BTF and BCF may be explained with 0.1–1.2 per cent of interconnected fluids (Hashin & Shtrikman 1962) associated with mafic material.

8.2. Narmada–Son lineament

The NE-SW structural trend of the NSL in the northern limit of the CITZ covers almost the entire peninsular India. It is characterized by rift faulted and upliftment with crustal warping (Choubey 1971). The fault-controlled volcanism and sedimentation lead to the formation of the MG supracrustal belt in the middle of the NSSF, and NSNF, the volcano-sedimentary rich formation represents the mantle-activated continental aborted rift (CRUMANSONATA 1995; Acharya & Roy 2000; Roy & Prasad 2003). Earlier MT studies in the western part of the NSL (Rao *et al.* 2004; Patro *et al.* 2005; Patro & Sarma 2016; Naganjaneyulu & Santosh 2010;

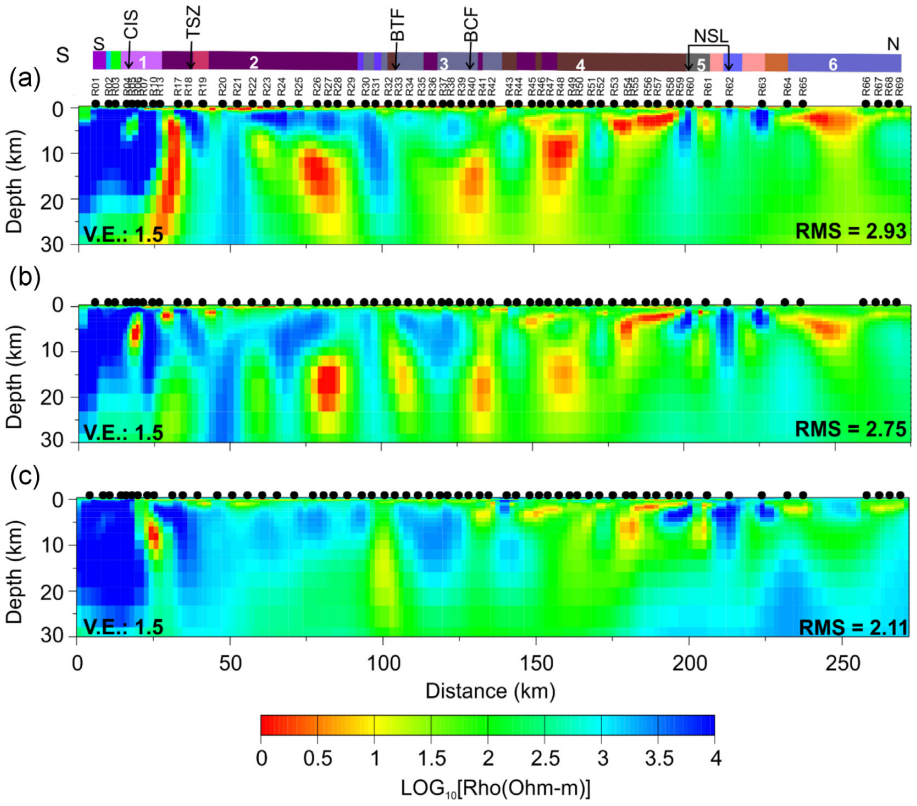

Figure 9: 3-D inversion results with background resistivities of 10, 100 and 1000 Ω-m in figures (a), (b) and (c), respectively. The model derived from 1000 Ω-m half-space has the minimum RMS (2.11) as compared to other models. The top panel shows the geology of the study area. 1: Peninsular gneiss, 2: Deccan trap, 3: Upper Gondwana, 4: Lower Gondwana, 5: Mahakoshal and 6: Vindhyan.

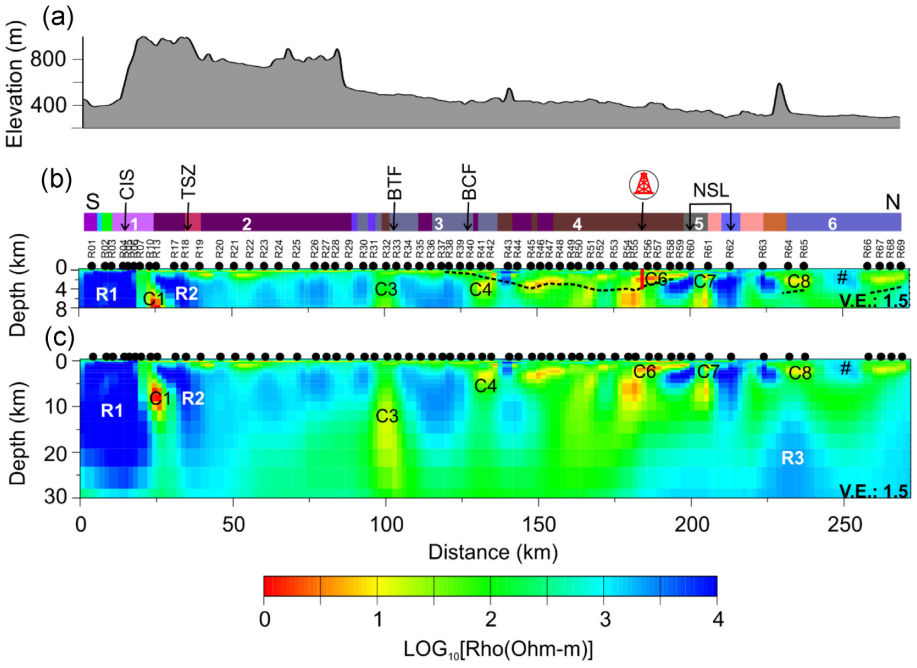

Figure 10: (a) Topography data (source: https://www.gmrt.org/GMRTMapTool/) along the profile from south to north. (b) Shallow geoelectric section derived from the 3-D inversion of both impedance and tipper data in the frequency range of 1000–0.001 Hz. The black colour dashed lines represent Gondwana and Vindhyan sediment thickness, which is derived from the 1-D inversion of the invariant component of impedance tensor. (c) 3-D deep geo-electrical section derived from the 3-D inversion of impedance and tipper data in the frequency range of 1000–0.001 Hz. The red colour vertical line in figure (b) indicates the thickness of the sediment derived from the Tikhi Borewell (Jitendra Kumar *et al.* 2005). The top panel shows the geology across the MT traverse. 1: Peninsular gneiss, 2: Deccan trap, 3: Upper Gondwana, 4: Lower Gondwana, 5: Mahakoshal and 6: Vindhyan. # denotes data gap in the profile.

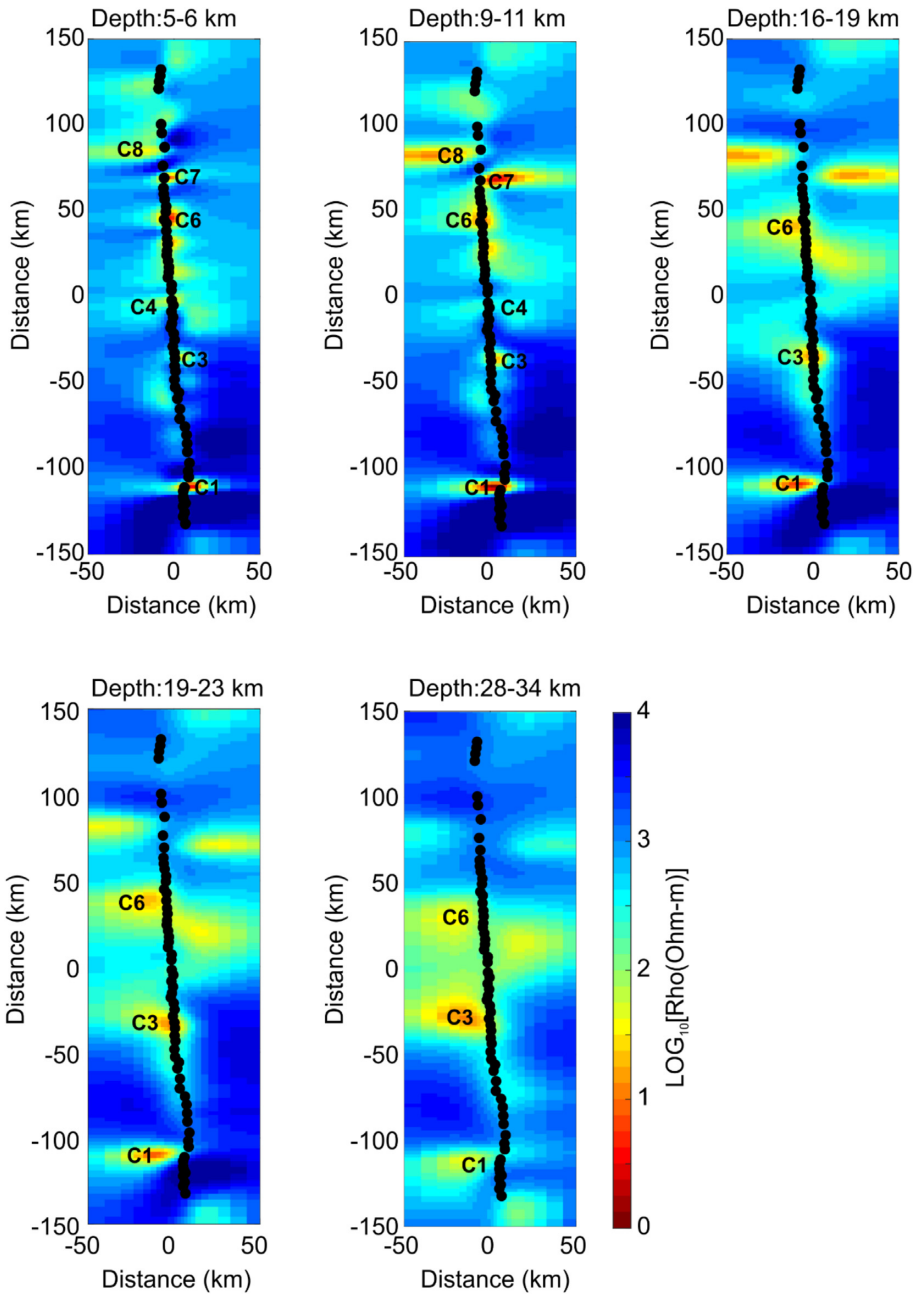

Figure 11: Horizontal resistivity section derived from 3-D inversion results at different depth ranges. MT stations are shown with a black colour circle. C1-C8 are the conductive features discussed in the text.

Abdul Azeez *et al.* 2013) note a high conductive structure in mid-lower crustal level and they suggest that the conductor could be associated with Deccan volcanic origin of mafic-ultramafic materials. However, this study delineates a conductor (C7 in Fig. 10b) at a shallow level in the middle of the NSSF, and NSNF that spatially coincide with the surface expression of MG rocks. Therefore, the conductor 'C7' may be associated with the sedimentary formation of MG. The present results also are well corroborate well with the previous gravity and electrical studies (CRUMANSONATA 1995) carried out in the western part of the present study.

In addition, the present 3-D model brought out a high resistive (> 1000 Ω-m in Fig. 10c) crustal structure below the NSL that marks a northern limit of the CITZ in the present study area. The structure may be connected with the high resistive lower crustal column R3. The intrusion of high resistivity and high-density rocks such as granite along the weak zones during the evolution of MG/NSL imprints in the form of horst type structure below the NSL. A similar kind of signature is observed below the NSL by the MT studies (Gokarn *et al.* 2001) in the western part of the present study area. The horst feature in the middle of the NSSF and NSNF forms as crustal uplifting (Murty *et al.* 2004). Later on, the intermittent reactivation of NSSF and NSNF brought out a graben structure on either side of the NSL, and the graben structure is received Gondwana and Vindhyan sediments in the south and northern parts of the NSL, respectively.

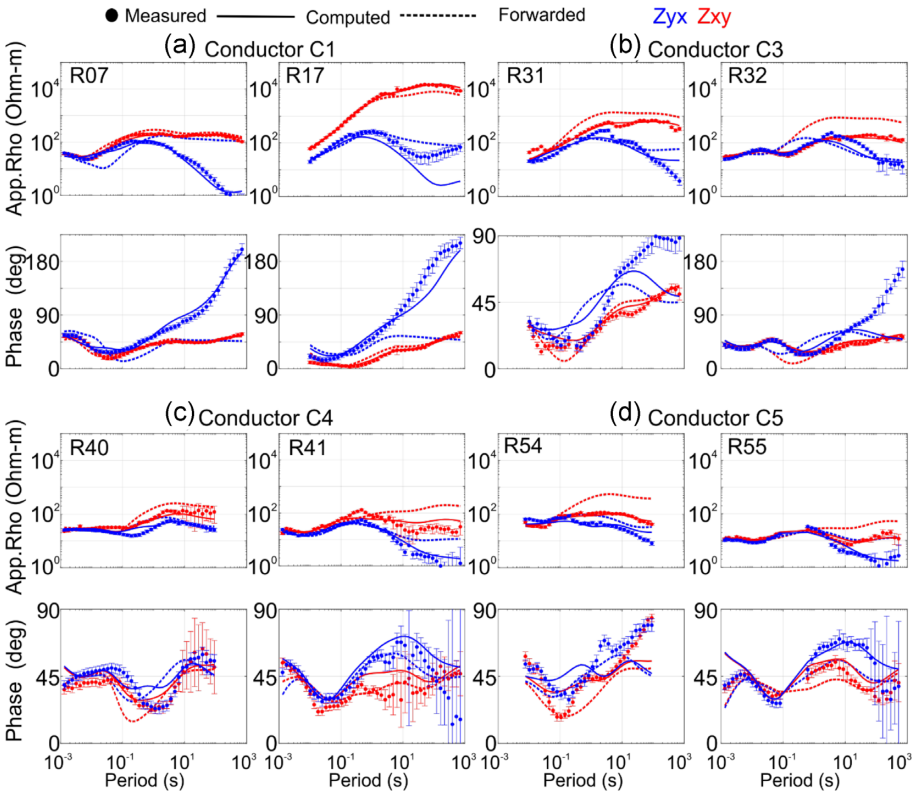

Figure 12: Sensitivity analysis results in figures (a), (b), (c) and (d) of conductive features C1, C3, C4 and C5, respectively, in the 3-D model.

8.3. Resistivity structure across CIS and TSZ

Despite several geological and geophysical studies conducted across CITZ, the subduction polarity and suture between the SIB and NIB are still ambiguous. Therefore, based on this study results we propose a hypothesis that can explain a possible mechanism for suturing of the SIB and NIB, further we discuss a possible cause of a high conductivity zone in the middle of the CIS and TSZ.

8.3.1. Central India Tectonic Zone

Geological (Jain &Yedekar 1989; Yedekar *et al.* 1990; Jain *et al.* 1991; Kumar Giri *et al.* 2021) and geophysical (Mishra *et al.* 2000) studies suggest that the CITZ is formed by suturing of NIB and SIB along the CIS during the Palaeoproterozoic in a simple monocycle model. However, petrological and geochronological studies (Bhowmik et al. 2005; Bhowmik 2019, and reference therein) propose a polycyclic model for the formation of the CITZ in the span of ∼1000 Ma. The tectonic activity in central India was initiated through the subduction of the oceanic lithosphere attached to the NIB below the SIB (∼1.62 Ga) that result in the formation of magmatic arc, that is, Tirodi Biotite Gneiss (TBG) and backarc domain, that is, Bhandara-Balaghat Granulite (BBG, Bhowmik 2019). The first phase of crustal deformation occurs through lithospheric extensional tectonics. Where the BBG belt is confronted multiple prograde metamorphisms attribute to multiple shear zones and mylonites. In addition, crustal structures on either side of the BBG are highly modified by the tectonic process. It underwent extension and compression within a short time that lead to marking of a suture zone, namely CIS between the arc (TBG) and backarc (BBG, Basu & Bhowmik 2008; Bhowmik *et al.* 2011; Ramachandra & Roy 2001). Later on, the area experienced another phase of extensional tectonics by the rollback of the subduction slab (Bhowmik et al. 2005). During this period, the Sausar basin is developed and filled with reworked basement gneissic rocks. The Sausar basin is separated from adjacent granulite belts, that is, BBG and Ramakona-Katangi Granulite (RKG) through the tectonic contacts where they mark with the ductile shear zones (Ramachandra & Roy 2001; Bhowmik & Roy 2003). The final suturing of the SIB and NIB occurred between the 1.06 and 0.93 Ga through the continued northward subduction of the SIB below the NIB that lead to oblique continental-continental-collision orogeny along the TSZ (Bhowmik *et al.* 2012; Chattopadhyay & Khasdeo 2011; Chattopadhyay *et al.* 2020). The continental collision lead to the closure of the Sausar basin and the formation RKG belt along the southern part of TSZ. Besides, the continental collision results in anomalous crustal thickening and lower crustal melting followed by decompression that lead to crustal removal (Bhowmik *et al.* 1999).

The above discussion indicates that the assembly of SIB and NIB occurs mainly at two stages, the southward subduction of oceanic lithosphere attached to the NIB followed by continued northward subduction of SIB induces oblique collision between the SIB and NIB. Thus, the CITZ could be formed through the transition of oceanic subduction to continental collision via multiple tectonic activities at different stages. The transition of southward subduction to continental collision lead to the closure of ocean basin in the middle of the SIB and NIB followed by thickening and upliftment (see Fig. 10a) of crustal rocks through the continental collision. During the evolution of CITZ, multiple extensional tectonics in central India generate fracture zones that act as precursors for multiple shear zones within the limit of the CIS and TSZ. The geometry and location of the shear zone are controlled by the initial stage of brittle fracture. Fluid rock interaction in the brittle fracture zone lead to the

formation of the ductile shear (deformation) zone that is noted as a conductor (C1) in the 3-D model (Fig. 10c). The deformation zone may be widened in the limit of two shear zones by the fluid–rock interaction such as metamorphic reactions (e.g. Segall & Simpson 1986; Mancktelowa & Pennacchioni 2005; Goncalves *et al.* 2016).

Many of the tectonic zones (related to subduction, collision, suture) are reflected as low resistive features in the resistivity image of the crustal column (e.g. Unsworth *et al.* 2000; Unsworth 2010; Worzewski *et al.* 2010; Patro *et al.* 2014; Abdul Azeez *et al.* 2017). The present 3-D resistivity model brought out a high conductive vertical feature in the middle of (C1 in Figs 10b and c) the CIS and TSZ, and that extends the entire crustal column with a resistivity range of 10 Ω-m in upper crustal level and ∼100 Ω-m in lower crustal level. Since the CIS and TSZ are close to each other in this study area compared to other parts, the crustal conductor C1 (Fig. 10c) obtained in the current 3-D model may represent the signature of both shear zones. A reflective crust beneath CIS is observed from the seismic studies carried out along a profile that is nearly 130 km away from the present profile in the SW direction (Mandal *et al.* 2013). MT study (Abdul Azeez *et al.* 2017) coinciding with the seismic profile of Mandal et al. (2013) delineated an upper crustal linear conductive feature to the north of CIS and a gently dipping conductor beneath TSZ extending through the crustal column. Due to the multiple tectonic events such as subduction, collision, and extensional tectonics in 1000 Ma (Bowmik 2019; Chatopadhya *et al.* 2020), the crustal structure could be deformed across the two shear zone through high-grade metamorphism. Multiple radial fractures of two shear zone overlap each other under extensional tectonics and develop a damage/deformation zone in the middle of the two shear zones. There could be a possibility of interaction between the two-shear zones as they are close to each other under the extensional tectonics, resulting in the formation of damage/deformations zone, hence, that could be an alternative explanation for the evolution of high conductivity in the middle of the two shear zones. Ancient tectonic markers such as southward subduction and an oblique collision in the CITZ might be obscured by reworked or recent tectonic activities, hence, we could image both shear zones together as damage/deformations zone rather than an individual signature of the CIS and TSZ in this study. As a final point, we suggest that the deformation zone which is observed by this study may be a boundary between the SIB and NIB.

8.3.2. Causes of high conductivity in the middle of the CIS and TSZ

Generally, the deformation zones are associated with faults, fractures, and deformation bands. Such zones are reflected as conductive regions in the MT models (Unsworth *et al.* 2000; Bedrosian *et al.* 2002; Becken & Ritter 2012), which image the fault zone conductors. The conductors are explained as interconnected fluid pathways in the upper crustal level and/or ductile shearing of conductive minerals such as graphite, sulphide and metallic oxide in the lower crustal level. The mineral grain boundaries are interconnected under the post-collisional shearing process that enhances the conductivity; however, which type of grain boundaries enhances the conductivity below the two shear zones is a crucial question.

Throughout the world, the MT studies across the ancient or inactive continental collision/subduction zones suggest that during the formation of the Laurentia supercontinent in Palaeo-Proterozoic (2–1.8 Ga) time, the Earth structure was mainly affected by collision and accretion along the suture zones. The suture zones allow pathways for mantle-derived fluids or melts and enrich the crustal structure with carbonaceous, sulfide or iron oxide minerals from subducted sediments. The mineral system transformed to the high crustal conductors such as sulfide, graphite and/or iron-rich rocks along the suture zones during the metamorphism and associated shear-related deformation (Jones 1993; Boerner *et al.* 1996; Nover 2005; Selway 2014; Unsworth 2010; Weckmann 2012; Bologna *et al.* 2017; Padilha *et al.* 2019). The high conductive feature (C1 in Fig. 10c) below the CIS and TSZ could be related to the continental collision process that joins the SIB and NIB through the subduction and collision process. The conductive feature (C1) also may indicate the southern limit of CITZ in this study area. Mylonites generally develop along the shear zones with high porosity, which could cause high conductivity below the shear zones. Seismic studies (Mandal *et al.* 2013) across the CIS in the western part of this study area noted mylonites' existence with fluids. However, in the lower crustal level, high pressure and temperature lead to decrease in the porosity and loss of aqueous fluids during the deformation (Yin *et al.* 2014); hence, we ruled out the presence of mylonite association fluid in the lower crustal level of the two shear zone. However, the high conductivity (∼10 Ω-m) at shallow level (C1 in Figs 10b and c) may be a cause of mylonite associated with fluids. Sulfide minerals are another possible cause of high conductivity in the lower crustal interconnected shear zones, but sulfides are unstable at greater depth (Selway 2014). Therefore, the presence of sulfide minerals in the lower crustal level of the CIS and TSZ is not possible.

Further, the graphite mineral is one of the abundant minerals in shear zones that can produce high conductivity along the shear zones (Ritter *et al.* 1999; Weckmann 2012). Graphite is stable at a temperature below 1100 °C, but grain boundary graphite films are stable only at a temperature of 600–900 °C (Becken & Ritter 2012; Yoshino & Noritake 2011; Selway 2014 and reference therein). The high-grade metamorphic events (temperature more than 1000 °C) during the collision process (Bhoumik 2019) do not support the existence of grain boundary graphite films in the crustal level of the two shear zones. Metallic oxides such as manganese and copper are another plausible conductivity mineral in ancient suture zones precipitated from oceanic sediments when the subduction of oceanic lithosphere below the continental lithosphere has taken place. In central India, the oceanic lithosphere initiates the SIB and NIB amalgamation by subduction below the continental lithosphere (e.g. Yedekar *et al.* 1990; Mandal *et al.* 2013; Abdul Azeez *et al.* 2017; Bhowmik 2019). Thus, the manganese-rich sediment could be precipitated during the collision process and emplaced on the surface via weak zones such as CIS and TSZ. The presence of manganese oxide ore minerals in the Sausar group of rocks in the middle of two shear zones strongly supports this assumption. Therefore, we infer that the manganese-rich sediment (Bhowmik 2019) could be one of the candidates for the high conductivity in the CIS and TSZ. Further, if we consider the Hashin–Shtrikman bound with resistivities of 0.1 Ω-m for the conductive fluids and 10 000 Ω-m for the resistive background, the ∼1.5 percent of interconnected fluid is required to match the observed resistivities (∼ 10 Ω-m).

9. CONCLUSIONS

The dense-spaced MT studies across the CITZ over the length of 275 km bought out the thickness variation of Gondwana and Vindhayan sediments and the electrical signature of crustal level shear zones. The formation of the NSL active rift zone results in the deposition

of Gondwana and Vindhyan sediments in the graben structure on either side of the NSL. The northward thrust of boundary faults and intrabasinal faults in the South-Rewa basin led to an increase of sediment thickness towards the north compared to the southern part. In the view of sediment thickness and tectonic setting of the Gondwana basin, the northern part of the basin is more hydrocarbon prospective than the southern region (Dotiwala & Pangtey 1997). Further, the shallow level of intrabasinal faults, that is, BTF and BCF in the South-Rewa basin, divide the basin into sub-basins and increase sediment thickness towards the north. The 3-D model brought out a conductive feature in the middle of the CIS and TSZ with a resistivity range of 10–100 Ω-m. The conductive feature could be related to the collision process in central India; it also indicates the boundary between the SIB and NIB. Collision-related metallic-rich sediments (Manganese could be a potential candidate, as it is found in the Sausar basin to the west of the study region) could be the cause of moderate conductivity (∼100 Ω-m) in lower crustal level. Mylonite or metallic-rich sediment associated with fluids may generate high conductivity (10 Ω-m) in the upper crustal level of two shear zones. Correlating this study results with earlier geophysical and geological studies, we finally suggest that the CITZ may be formed through the transition of southward subduction of oceanic lithosphere attached to the NIB to northward subduction of SIB-induced oblique continental collision.

ACKNOWLEDGMENTS

We thank Director CSIR-NGRI for the constant encouragement and permission to publish this work. We are also thankful to Sivamallaiah Sana and Vaddeboina Suresh for participating in MT data acquisition. PKP thanks Alan Jones for providing the strike code and Gary Egbert for providing the ModEM code. PKP also thanks Naser Meqbel for sharing 3-D Grid software. The study was supported by a CSIR 12th five year plan project SHORE (PSC-0205) and MLP-6404-28 (BPK). Khasi Raju also acknowledges CSIR for supporting his research through the CSIR—Senior Research Fellowship. We profoundly thank both the reviewers and editor Ute Weckmann for their comments which have helped in improving the manuscript.

DATA AVAILABILITY

Data used for the study are available with CSIR—National Geophysical Research Institute and can be made available with the consent of the corresponding author under the institutional data policy.

REFERENCES

Azeez, Abdul, K., K., Unsworth, M. J., Patro, P. K., Harinarayana, T. & Sastry, R. S, 2013. Resistivity structure of the Central Indian Tectonic Zone (CITZ) from Multiple Magnetotelluric (MT) profiles and tectonic implications, *Pure appl. Geophys.,* **170,** 2231–2256.

Azeez, Abdul, K., K., Patro, P.K., Harinarayana, T. & Sarma, S.V.S., 2017. Magnetotelluric imaging across the tectonic structures in the eastern segment of the Central Indian Tectonic Zone: preserved imprints of polyphase tectonics and evidence for suture status of the Tan Shear, *Precambrian Res.,* **298,** 325–340.

Acharyya, S. K. & Roy, A., 2000. Tectonothermal history of the central Indian tectonics zone and reactivation of major faults/shear zone, *J. geol. Soc. India,* **55**(3), 239–256.

Acharyya, S. K., 2003. The nature of Mesoproterozoic Central Indian Tectonic Zone with exhumed and reworked older granulites, *Gondwana Res.,* **6**(2), 197–214.

Acharyya, S. K., 2019. Tectonic setting and Gondwana Basin architecture in the Indian shield, Acharyya, S. K.(ed). *Developments in Structural Geology and Tectonics,* Elsevier. Vol. **4,** pp. 1–139.

Bahr, K., 1988. Interpretation of the magnetotelluric impedance tensor: regional induction and local telluric distortion, *J. geophys.,* **62,** 119–127.

Bahr, K., 1991. Geological noise in magnetotelluric data: a classification of distortion types, *Phys. Earth planet. Int.,* **66,** 24–38.

Basu, S. A. & Bhowmik, S. K., 2008. Constraining the metamorphic evolution of a cryptic hot Mesoproterozoic orogen in the Central Indian Tectonic Zone, using P-T pseudosection modeling of mafic intrusions and hot reworked granulites, *Precambrian Res.,* **162,** 128–149.

Beamish, D. & Travassos, J.M., 1992. The use of the D + solution in magnetotelluric interpretation, *J. appl. Geophys.,* **29,** 1–19.

Becken, M. & Ritter, O., 2012. Magnetotelluric studies at the San Andreas Fault Zone: implications for the role of fluids, *Surv. Geophys.,* **33,** 65–105.

Bedrosian, P, A., Unsworth, M, J. & Egbert, G., 2002. Magnetotelluric imaging of the creeping segment of the San Andreas Fault near Hollister, *Geophys. Res. Lett.,* **29**(11), 1506–1509.

Bhattacharji, S., Chatterjee, N., Wampler, J. M., Nayak, P.N. & Deshmukh, S. S., 1996. Indian intraplate and continental margin rifting, lithospheric extension, and mantle upwelling in Deccan flood Basalt volcanism near the K/T boundary: evidence from Mafic dyke swarms, *J. Geol.,* **104,** 379–398.

Bhowmik, S. K., Pal, T., Roy, A. & Pant, N. C., 1999. Evidence for Pre-Grenvillian high-pressure granulite metamorphism from the northern margin of the Sausar mobile belt in Central India, *J. geol. Soc. India,* **53,** 385–399.

Bhowmik, S. K. & Roy, A., 2003. Garnetiferous metabasites from the Sausar Mobile Belt: Petrology, P-T path and implications for the tectonothermal evolution of the Central Indian Tectonic Zone, *J. Petrol.,* **44,** 387–420.

Bhowmik, S. K., Sarbadhikari, A. B., Spiering, B. & Raith, M. M., 2005. Mesoproterozoic reworking of Palaeoproterozoic ultrahigh-temperature granulites in the Central Indian Tectonic Zone and its implications, *J. Petrol.,* **46,** 1085–1119.

Bhowmik, S. K., Wilde, S. A. & Bhandari, A., 2011. Zircon U-Pb/Lu-Hf and monazite chemical dating of the Tirodi biotite gneiss: implication for latest Palaeoproterozoic to Early Mesoproterozoic orogenesis in the Central Indian Tectonic Zone, *Geol. J.,* **46,** 574–596.

Bhowmik, S. K., Wilde, S. A., Bhandari, A., Pal, T. & Pant, N. C., 2012. Growth of the Greater Indian landmass and its assembly in Rodinia: geochronological evidence from the Central Indian Tectonic Zone, *Gondwana Res.,* **22,** 54–72.

Bhowmik, S.K., 2019. The current status of orogenesis in the Central Indian Tectonic Zone: a view from its Southern Margin, *Geol. J.,* **54,** 2912–2934.

Borah, U.K., Patro, P.K. & Suresh, V., 2015. Processing of noisy magnetotelluric time series from Koyna-Warna seismic region, India: a systematic approach, *Ann. Geophys.,* **58**(2), G0222.

Boerner, D.E., Kurtz, R.D. & Craven, J.A., 1996. Electrical conductivity and Paleo Proterozoic foredeeps, *J. geophys. Res.,* **101**(13), 775–13.

Bologna, M.S., Egbert, G.D., Padilha, A.L., Pádua, M.P. & Vitorello, I., 2017. 3-Dinversion of complex magnetotelluric data from an Archean-Proterozoic terrain in northeastern São Francisco Craton, Brazil, *Geophys. J. Int.,* **210,** 1545–1559.

Bostick, F. X., 1977. A simple almost exact method of MT analysis: workshop on electrical methods in geothermal exploration, *U.S. Geological Survey,* Contract No. 14080001–8 359 174–183.

Caldwell, T. G., Bibby, H.M. & Brown, C., 2004. The magnetotelluric phase tensor, *Geophys. J. Int.,* **158,** 457–469.

Camfield, P. A. & Gough, D.I., 1977. A possible Proterozoic plate boundary in North America, *Can. J. Earth Sci.,* **14,** 1229–1238.

Casshyap, S.M., Tewari, R.C. & Khan, A., 1993. Alluvial fan origin of Bagra formation (Mesozoic Gondwana) and tectonostratigraphic implications, *J. geol. Soc. India,* vol. **42,** pp. 269–279.

Chakraborty, C., Mandal, N. & Ghosh, S.K., 2003. Kinematics of the Gondwana basins of peninsular India, *Tectonophysics,* **377,** 299–324.

Chakraborty, C., 2006. Proterozoic intracontinental basin: the Vindhyan example, *J. Earth Syst. Sci.,* **115**(1), 3–22.

Chattopadhyaya, A & Bhattacharjee, D, 2019. Repeated reactivation of the Gavilgarh-Tan Shear Zone, Central India: implications for the tectonic survival of deep-seated intra-continental fault zones, *J. Asian Earth Sci.,* **186,** 104051.

Chattopadhyay, A. & Khasdeo, L., 2011. Structural evolution of Gavilgarh-Tan Shear Zone, central India: a possible case of partitioned transpression during Mesoproterozoic oblique collision within Central Indian Tectonic Zone, *Precambr. Res.,* **186,** 70–88.

Chattopadhyay, A., Bhowmik, S. K. & Roy, A., 2020. Tectonothermal evolution of the Central Indian Tectonic Zone and its implications for Proterozoic supercontinent assembly: the current status, *Episodes,* **43**(1), 132–144.

Chave, A.D. & Jones, A.G., 2012. *The Magnetotelluric Method: Theory and Practice,* Cambridge University Press, New York, p. 570.

Choubey, V. D., 1971. Narmada-Son Lineament, India, *Nat. Phys. Sci.,* **232,** 38–40.

Constable, S.C., Parker, R.L. & Constable, C.G., 1987. Occam's inversion: a practical algorithm for generating smooth models from electromagnetic sounding data, *Geophysics,* **52,** 289–300.

CRUMANSONATA. 1995. Geoscientific studies of the Son–Narmada–Tapti Lineament Zone, *Geol. Soc. India. Spec. Publ.,* **10,** 1–371.

Cruces-Zabala, J., Ritter, O., Weckmann, U., Tietze, K. & Schmitz, M., 2020. Magnetotelluric imaging of the Mérida Andes and surrounding areas in Venezuela, *Geophys. J. Int.,* **222**(3), 1570–1589.

Dotiwala, S. & Pangtey, K.K.S., 1997. Structural setting and Hydrocarbon prospects of the Son-Mahanadi basin, India—emphasis on the Son graben, *Bull. Oil Natural Gas Corp. Limited,* **34**(1), 81–97.

Egbert, G.D., 1990. Comments on 'Concerning dispersion relations for the magnetotelluric impedance tensor, by Yee, E. & Paulson, K.V., *Geophys. J. Int.,* **102,** 1–8.

Egbert, G. D. & Kelbert, A., 2012. Computational recipes for electromagnetic inverse problems, *Geophys. J. Int.,* **189,** 251–267.

Frost, B. R. & Bucher, K., 1994. Is water responsible for geophysical anomalies in the deep continental crust? A petrological perspective, *Tectonophysics,* **231,** 293–309.

Frost, B.R. & Frost, C.D., 1987. CO2, melts, and granulite metamorphism, *Nature,* **327,** 503–506.

Gamble, T.D., Goubau, W.M. & Clarke, J., 1979. Magnetotellurics with remote magnetic reference, *Geophysics,* **44,** 53–68.

George, B.G. & Ray., S. J, 2020. Depositional history of the Mesoproterozoic Chhattisgarh Basin, central India: insights from geochemical provenance of siliciclastic sediments, *Int. Geol. Rev.,* **63**(3), 380–395.

Gokarn, S. G., Rao, C. K., Gupta, G., Singh, B. P. & Yamashita, M., 2001. Deep crustal structure in central India using magnetotelluric studies, *Geophys. J. Int.,* **144,** 685–694.

Goncalves, P., Poilvet, J.C., Oliot, E., Trap, P. & Marquer, D., 2016. How does shear zone nucleate? An example from the Suretta nappe (Swiss Eastern Alps), *J. Struct. Geol.,* **86,** 166–180.

GSI, 2005. Geological and mineral map of Madhya Pradesh and Chhattisgarh, Geological Survey of India, India.

Hashin, Z. & Shtrikman, S., 1962. A variational approach to the theory of the effective magnetic permeability of multiphase materials, *J. Appl. Phys.,* **33**(10), 3125–3131.

Heise, W. & Pous, J., 2003. Anomalous phases exceeding 90° in magnetotellurics: anisotropic model studies and a field example, *Geophys. J. Int.,* **155**(1), 308–318.

Hering, P., Brown, C. & Junge, A., 2019. Magnetotelluric apparent resistivity tensors for improved interpretations and 3-D inversions, *J. geophys. Res.: Solid Earth,* **124,** 7652–7679.

Ichihara, H. & Mogi, T., 2009. A realistic 3-D resistivity model explaining anomalous large magnetotelluric phases: the L-shaped conductor model, *Geophys. J. Int.,* **179,** 14–17.

Jain, S.C. & Yedekar, D.B., 1989. A note on geological traverses in Nagpur-Balaghat-Bilaspur-Raigarh area, Maharastra and Madhya Pradesh for marking the extension of central India shear/suture zone, *Rec.Geol. Surv. India,* **122**(6),181–183.

Jain, S. C., Yedekar, D. B. & Nair, K. K. K., 1991. Central Indian Shear Zone: a major Pre-Cambrian crustal boundary, *J. geol. Soc. India,* **37,** 521–531.

Kumar, Jitendra, Singh, Paramjit, Verma, N. K. & Negi, M. S., 2005. Modelling of igneous-prone south Rewa basin an integrated approach, in *Proceedings of 6th International Petroleum Conference and Exhibition, 15–19 January,* New Delhi, pp. 1–6.

Jones, A.G., 1983. On the equivalence of the ''Niblett" and ''Bostick" transformations in the magnetotelluric method, *J. geophys.,* **53,** 72–73.

Jones, A.G., 1992. Electrical conductivity of the lower continental crust, in: Fountain, D.M., Arculus, R. & Kay, R. W.(eds), *Continental Lower Crust. (Developments in Geotectonics),* Vol. **23**(1), Elsevier, Amsterdam, pp. 81–143.

Jones, A.G., 1993. Electromagnetic images of modern and ancient subduction zones, *Tectonophysics,* **219,** 29–45.

Kaila, K.L., Murty, P.R.K., Mall, D.M., Dixit, M.M. & Sarkar, D., 1987. Deep seismic soundings along Hirapur-Mandla profile, central India, *Geophys. J. R. astron. Soc.,* **89,** 399–404.

Kelbert, A., Meqbel, N., Egbert, G. D. & Tandonc, K., 2014. ModEM: a modular system for inversion of electromagnetic geophysical data, *Comput. Geosci.,* **66,** 40–53.

, Hjelt, S.E, 1993. Electromagnetic studies in the Fennoscandian Shield—electrical conductivity of Precambrian crust, *Phys. Earth planet. Inter.,* **81,** 107–138, doi.org/10.1016/0031-9201(93)90127-U.

Kumar Giri, R., Chalapathi Rao, N. V., Rahaman, W., Kumar, A., Satyanarayanan, M. & Keshav Krishna, A., 2021. Paleoproterozoic calc-alkaline lamprophyres from the Sidhi Gneissic complex, India: implications for plate tectonic evolution of the Central Indian Tectonic Zone, *Precambrian Res.,* **362,** 106316.

Kumar, S. & M., Sharma, *Vindhyan Basin, Son Valley area, Central India,* 2012. The Palaeontological Society of India, p. 145.

Lala, T., Choudhary, A.K., Patil, S.K. & Paul, D.K., 2011. Mafic Dykes of Rewa Basin, Central India: implications on magma dispersal and petrogenesis, Srivastava, R.K., (ed.), *Dyke Swarms: Keys for Geodynamic Interpretation,* Springer-Verlag Berlin Heidelberg, p. 141–165.

Livelybrooks, D., Mareschal, M., Blais, E. & Smith, J.T., 1996, Magnetotelluric delineation of the Trillabelle massive sulfide body in Sudbury, *Ontario. Geophys.,* **61,** 971–986.

Mall, D. M., Reddy, P.R. & Mooney, W.D., 2008. Collision tectonics of the central Indian suture zone as inferred from a deep seismic sounding study, *Tectonophysics,* **460,** 116–123.

Mandal, B., Sen, M. K. & Rao, V. V., 2013. New seismic images of the Central Indian Suture Zone and their tectonic implications, *Tectonics,* **32,** 908–921.

Mancktelow, N.S. & Pennacchioni, G., 2005. The control of precursor brittle fracture and fluid–rock interaction on the development of single and paired ductile shear zones, *J. Struct. Geol.,* **27,** 645–661.

Martı, ´ A, Queralt, P. & Ledo, J., 2009. WALDIM: a code for the dimensionality analysis of magnetotelluric data using the rotational invariants of the magnetotelluric tensor, *Comput. Geosci.,* **35,** 2295–2303.

Marti, A., 2014. The role of electrical anisotropy in magnetotelluric responses: from modelling and dimensionality analysis to inversion and interpretation, *Surv. Geophys.,* **35,** 179–218, doi.org/10.1007/s10712-013-9233-3.

Merle, O., 2011. A simple continental rift classification, *Tectonophysics,* **513,** 88–95.

Mishra, D. C., Singh, B., Tiwari, V. M., Gupta, S. B. & Rao, M. B. S. V., 2000. Two cases of continental collision and related tectonics during the Proterozoic period in India — insights from gravity modeling constrained by seismic and magnetotelluric studies, *Precambrian Res,* **99,** 149–169.

Mukherjee, D., Ray, S., Chandra, S., Pal, S. & Bandyopadhyay, S., 2012. Upper Gondwana succession of the Rewa basin, India: understanding the interrelationship of lithologic and stratigraphic variables, *J. geol. Soc. India,* **79,** 563–575.

Murty, A. S. N., Tewari, H. C. & Reddy, P. R., 2004. 2-D crustal velocity structure along Hirapur-Mandla profile in central India: an update, *Pure appl. Geophys.,* **161**(1), 165–184.

Naganjaneyulu, K. & Santhosh, M., 2010. The Central Indian Tectonic Zone: a geophysical perspective on continental amalgamation along a Mesoproterozoic suture, *Gondwana Res,* **18,** 547–564.

Naidu, G. D. & Harinarayana, T., 2009. Deep electrical imaging of the Narmada-Tapti region, central India from magnetotellurics, *Tectonophysics,* **476,** 538–549.

Naqvi, S. M., Divakara Rao, V. & Narain, H., 1974. The proto continental growth of the Indian Shield and the antiquity of its rift valleys, *Precambrian Res.,* **1**(4), 345–398.

Nover, G., 2005. Electrical properties of crustal and mantle rocks—A review of laboratory measurements and their explanation, *Surv. Geophys.,* **26,** 593–651.

Ogawa, Y., 2002. 'On two-dimensional modeling of magnetotelluric field data', *Surv. Geophys,* **23,** 251–273.

Padilha, A.L., Vitorello, I., Pádua, M. & Fuck, R.A., 2019. Magnetotelluric images of Paleoproterozoic accretion and Mesoproterozoic to Neoproterozoic reworking processes in the northern São Francisco Craton, central-eastern Brazil, *Precambrian Res,* **333,** 105416, doi: 10.1016/j.precamres.2019.105416.

Parker, R.L., 1983. The magnetotelluric inverse problem, *Geophys. Surv.,* **6,** 5–25.

Patro, B. P. K., Harinarayana, T., Sastry, R. S., Rao, M., Manoj, C., Naganjaneyulu, K. & Sarma, S.V.S., 2005. Electrical imaging of Narmada-Son Lineament Zone, Central India from magnetotellurics, *Phys. Earth planet. Inter.,* **148,** 215–232.

Patro, P. K., Sarma, S. V. S. & Naganjaneyulu, K., 2014. Three-dimensional lithospheric electrical structure of Southern Granulite Terrain, India and its tectonic implications, *J. geophys. Res.—Solid Earth,* **119,** 71–82.

Patro, P.K. & Sarma, S.V.S., 2016. Evidence for an extensive intrusive component of the Deccan Large Igneous Province in the Narmada Son Lineament region, India from three-dimensional magnetotelluric studies, *Earth planet. Sci. Lett.,* **451,** 168–176.

Pous, J., Munoz, G., Heise, W., Melgarejo, J.C. & Quesada, C., 2004. Electromagnetic imaging of Variscan crustal structures in SW Iberia: the role of interconnected graphite, *Earth planet. Sci. Lett,* **217,** 435–450.

Raju, K & Patro, P. K, 2020. Dimensionality analysis of MT data using Mohr circle: a case study from Rewa–Shahdol region, *India. J. Earth Syst. Sci.,* **129,** 9, doi.org/10.1007/s12040-019-1272-901234567.

Ramachandra, H. M. & Roy, A., 2001. Evolution of Bhandara-Balaghat granulite belt along the southern margin of the Sausar Mobile Belt of Central India, *Proc. Indian Acad. Sci. (Earth Planetary Science),* **110,** 351–368.

Rao, B.N., Kumar, N., Singh, A.P., Prabhakar Rao, M.R.K., Mall, D.M. & Singh, B., 2011. Crustal density structure across the Central Indian Shear Zone from gravity data, *J. Asian Earth Sci.,* **42,** 341–353.

Rao, C. K., Gokarn, S.G. & Singh, B. P., 1995. Upper crustal structure in the Tomi-Purnad region, Central India, using magnetotelluric studies, *J. Geomag. Geoelectr.,* **47,** 411–420.

Rao, C.K., Ogawa, Y., Gokarn, S.G. & Gupta, G., 2004. Electromagnetic imaging of magma across the Narmada Son lineament, central India, *Earth Planets Space,* **56,** 229–238.

Ritter, O., Haak, V., Rath, V., Stein, E. & Stiller, M., 1999.Very high electrical conductivity beneath the Munchberg Gneiss area in Southern Germany: implications for horizontal transport along shear planes, *Geophys. J. Int.,* **139**(1), 161–170.

Rodi, W. & Mackie, R. L., 2001. Nonlinear conjugate gradients algorithm for 2-D magnetotelluric inversion, *Geophysics,* **66,** 174–187.

Roy, A. & Prasad, M.H., 2001. Precambrian of Central India: a possible tectonic model, *Geol. Surv. India Spec. Publ.,* **64,** 177–197.

Roy, A. & Prasad, M. H., 2003.Tectonothermal events in Central Indian Tectonic Zone (CITZ) and its implications in Rodinian crustal assembly, *J. Asian Earth Sci.,* **22,** 115–129.

Ruppel, C., 1995. Extensional processes in continental lithosphere, *J. geophys. Res.,* **100**(B12), 24187–24215.

Segall, P. & Simpson, C., 1986. Nucleation of ductile shear zones on dilatant fractures, *Geology,* **14,** 56–59.

Selway, K., 2014. On the causes of electrical conductivity anomalies in tectonically stable lithosphere, *Surv. Geophys.,* **35,** 219–257.

Sensarma, S., Hoernes, S. & Mukhopadhyay, D., 2004. Relative contributions of crust and mantle to the origin of the Bijli Rhyolite in a palaeoproterozoic bimodal volcanic sequence (*Dongargarh Group*), central India, *Proc. Indian Acad. Sci. (Earth Planet. Sci.),* **113**(4), 619–648.

Sharma, U.P., Shukla, S., Sinha, K., Purohit, R.K., Majumdar, A. & Rai, A.K., 2014. Uranium occurrence in Proterozoic Chilpi Group, near Kanhari, Kawardha district, Chhattisgarh, *Current Sci.,* **107**(3), 364–366.

Simpson, F. & Bahr, K., 2005. *Practical Magnetotellurics,* Cambridge University Press, Cambridge.

Siripunvaraporn, W., Egbert, G. & Uyeshima, M., 2005. Interpretation of two-dimensional magnetotelluric profile data with three-dimensional inversion: synthetic examples, *Geophys. J. Int.,* **160,** 804–814.

Srivastava, A.K. & Mankar, R.S., 2015. Lithofacies architecture and depositional environment of Late Cretaceous Lameta Formation, central India, *Arab. J. Geosci,* **8,** 207–226.

Ting, S.C. & Hohmann, G.W., 1981. Integral equation modeling of three-dimensional magneto-telluric response, *Geophysics,* **46,** 182–197.

Unsworth, M. J., Bedrosian, P., Eisel, M., Egbert, G. & Siripunvaraporn, W., 2000. Along strike variations in the electrical structure of the San Andreas Fault at Park field, California, *Geophys. Res. Lett.,* **27**(18), 3021–3024.

Unsworth, M. J., Jones, A. G., Wei, W., Marquis, G., Gokarn, S. G. & Spratt, J. E., & the INDEPTH-MT team, 2005. Crustal Rheology of the Himalaya and Southern Tibet inferred from magnetotelluric data, *Nature,* **438,** 78–81.

Unsworth, M., 2010. Magnetotelluric studies of active continent-continent collisions, *Surv. Geophys.,* **31,** 137–161.

Weckmann, U., Ritter, O. & Haak, V., 2003a. Images of the magnetotelluric apparent resistivity tensor, *Geophys. J. Int.,* **155,** 456–468.

Weckmann, U., Ritter, O. & Haak, V., 2003b. A magnetotelluric study of the Damara Beltin Namibia: 2. MT phases over 90 reveal the internal structure of the Waterberg Fault/Omaruru Lineament, *Phys. Earth planet. Inter.,* **138,** 91–112.

Weckmann, U., 2012. Making and breaking of a continent: following the scent of geodynamic imprints on the African Continent using electromagnetics, *Surv. Geophys.,* **33**(1), 107–134, doi.org/10.1007/s10712-011-9147-x.

Weidelt, P. & Kaikkonen, P., 1994. Local 1-D interpretation of magnetotelluric B-polarization impedances, *Geophys. J. Int.,* **117,** 733–748.

Weidelt, P., 1999. 3D conductivity models, Implications of electrical anisotropy, in Oristaglio, M. J. & Spies, B. R.(eds.), *Three Dimensional Electromagnetics, S.E.G. Geophysical Developments Series,* Society of Exploration of Geophysicists, Vol. **7,** pp. 119–137.

West, W. D., 1962. The line of Narmada-Son valley, *Curr. Sci.,* **31,** 143–144.

Worzewski, T., Jegen, M., Kopp, H., Brasse, H. & Castillo, W.T., 2010. Magnetotelluric image of the fluid cycle in the Costa Rican subduction zone, *Nat. Geosci.,* **4,** 108–111.

Yedekar, D. B., Jain, S. C., Nair, K. K. K. & Dutta, K. K.(1990). The central Indian collision suture, in *Precambrian of Central India: Geol. Surv. India, Spec. Publ.,* (28), p. 1–43.

Yin, Y., Unsworth, M., Liddell, M., Pana, D. & Craven, J.A., 2014. Electrical resistivity structure of the Great Slave Lake shear zone, northwest Canada: implications for tectonic history, *Geophys. J. Int.,* **199**(1), 178–199.

Yoshino, T. & Noritake, F., 2011. Unstable graphite films on grain boundaries in crustal rocks, *Earth planet. Sci. Lett.,* **306**(3–4), 186–192.

SUPPORTING INFORMATION

Supplementary data are available at *GJI* online.

Please note: Oxford University Press is not responsible for the content or functionality of any supporting materials supplied by the authors. Any queries (other than missing material) should be directed to the corresponding author for the article.